



## City Research Online

### City, University of London Institutional Repository

---

**Citation:** Raffaele, B., Rodriguez Fernandez, C., Karathanassis, I. K. & Gavaises, M. (2023). Collapse of Cavitation Bubble Clusters of Fuels Utilised with Modern Combustion Systems. In: Ragucci, R., Marengo, M. & Sorrentino, G. (Eds.), ILASS Europe 2023 Meeting European Meeting on Liquid Atomization and Spray Systems. . Napoli, Italy: UNSPECIFIED. ISBN 978-88-88104-28-7

This is the accepted version of the paper.

This version of the publication may differ from the final published version.

---

**Permanent repository link:** <https://openaccess.city.ac.uk/id/eprint/32500/>

**Link to published version:**

**Copyright:** City Research Online aims to make research outputs of City, University of London available to a wider audience. Copyright and Moral Rights remain with the author(s) and/or copyright holders. URLs from City Research Online may be freely distributed and linked to.

**Reuse:** Copies of full items can be used for personal research or study, educational, or not-for-profit purposes without prior permission or charge. Provided that the authors, title and full bibliographic details are credited, a hyperlink and/or URL is given for the original metadata page and the content is not changed in any way.

---

City Research Online:

<http://openaccess.city.ac.uk/>

[publications@city.ac.uk](mailto:publications@city.ac.uk)

---

# Collapse of Cavitation Bubble Clusters of Fuels Utilised with Modern Combustion Systems

Raffaele Bellini, Carlos Rodriguez, Ioannis K. Karathanassis\*,  
Manolis Gavaises

School of Science & Technology, City, University of London, UK

\*Corresponding author: [Ioannis.Karathanassis@city.ac.uk](mailto:Ioannis.Karathanassis@city.ac.uk)

## Abstract

Cavitation and cavitation-induced erosion depend on fuel properties and working conditions. The majority of studies on cavitation consider simple thermodynamic Equations of State (EoS), which limit the analysis of thermal effects associated with the high pressure and temperatures occurring during bubble collapses. This can affect simulation fidelity, particularly when comparing fuels with different thermodynamic properties. The goal of this work is to examine, with the use of a real-fluid thermodynamic model, both pressure peaks and thermal effects owing to cavitation collapse of a cluster of vapour bubble at conditions prevailing in the fuel flow path inside modern fuel injectors; the selected conditions correspond to injectors utilised with Dual Fuel Internal Combustion Engines (DFICEs), using the properties of three different fuels for obtaining insights on how the cavitation cloud is developing during its collapse. The fuel's properties are exported on a structured table, which has been derived from the Helmholtz Energy EoS. This table is incorporated into an explicit density-based solver, using a Mach-consistent numerical flux for subsonic up to supersonic flow conditions. Evaluation of the developed solver is performed initially against benchmark cases reported in the open literature. Following the results from the selected fuels are compared and most evident differences are discussed.

## Introduction

As electrification for aviation, marine, heavy duty and earth moving vehicles is challenging, in an effort to mitigate the inevitable greenhouse gas emissions, partial substitution of Diesel with carbon-free or synthetic fuels in the so-called dual fuel internal combustion engines (DFICE), represents a promising alternative, see recent reviews [1,2]. In DFICEs, cavitation-induced erosion is still a persisting issue. Particularly for simulation approaches, the complexity in taking into account the properties of the mixtures of fuels and their variation across the range of operating conditions, represents an additional complexity. Cavitation-induced erosion causes material loss and degradation of hydraulic systems such as pumps, turbines, injectors, and ship propellers, see indicatively studies from the authors [3-7]. Experimental measurements of cavitating flows in true-scale fuel injectors are reported 25 years back [8-10] but they are still challenging, owing to the spatial and temporal resolutions required for capturing the very fast flow within the nozzle orifices. For that reason, parallel to experimental investigations, numerical modelling of cavitating flows has shown considerable progress since the '90s and continue in recent years, see indicatively [11-14]. However, cavitating flows include a vast range of spatial and temporal scales, sometimes accompanied by other processes (i.e. turbulence, heat transfer, chemical reactions, acoustic waves, erosion) rendering simulations computationally expensive; currently there is no universal Computational Fluid Dynamics (CFD) approach with sufficient accuracy suitable for the variety of technological applications where cavitation is realised.

Out of the various relevant numerical methods that are used today, three relevant to the current work are outlined here. The first model is referred to as Finite Mass Transfer (FMT) rate method; the multiphase flow is treated as a homogeneous mixture. The continuity and momentum equations are used to calculate the mixture flow, while an additional transport equation is utilised to capture the liquid-vapor interface. This transport equation can be based on the volume fraction VOF [15-17] of the two phases [18], through a level-set method [19] or even considering a two-fluid model [20]. In addition, the mass transfer between the liquid and vapour (cavitating) phases is estimated via an explicit source term added to the vapour transport equation. Most phase-change rate models in literature [21] are based on a simplified form of the Rayleigh-Plesset equation of bubble dynamics [22]; typically, the second temporal derivative of bubble radius as well as the effect of non-condensable gases are ignored. Empirical tuning constants are utilised to adjust the mass transfer rate between the liquid and the vapour phases. The non-universal values of these constants is one of the limitations of the FMT approach. It can be also noted that this model has been utilised irrespectively of the incompressible or compressible flow assumption; however, the authors have shown that considering fluid compressibility in the pressure-velocity correction equation may lead to ill-conditioned matrices of coefficients, which can cause numerical issues when large time steps are employed.

The second type of numerical approaches that has been utilised is the Discrete Bubble Model (DBM) [25,26]. According to this methodology, representative cavitation bubbles are tracked in a Lagrangian framework, while the

continuum flow is calculated using the flow governing equations solved in a Eulerian framework. Bubble-bubble interactions, fragmentation processes as well as turbulence flow effects on bubble trajectory and size response to local pressure dynamics, can be considered. Unfortunately, DBMs are limited to very low volume fractions, the weak (explicit in time) coupling between the two phases and the inherent assumption of spherical bubbles. To overcome these limitations, hybrid multi-scale models have been developed. In such approaches, larger cavities are represented using a transport equation model, while small-scale structures are tracked in an Lagrangian framework. In particular, the study of [27] has demonstrated the capability to estimate the dynamics of collapsing bubbles via the coupling of an Eulerian, finite mass-transfer model and a Lagrangian model. In their model, the vapor-liquid mixture properties are obtained based on a volume fraction methodology, in which cavities are tracked in the Lagrangian framework rather than solving an Eulerian transport equation. In general, Lagrangian models (or Hybrid Lagrangian Models) have a less precise estimation of the liquid-vapor interface compared to the fully Eulerian models, while, depending on the conditions, they may be sensitive to the initial assumptions made for the nuclei size and their number density.

In the last group, the two-phase cavitation regime is considered as a single fluid flow under the assumption of mechanical and thermodynamic equilibrium. This equilibrium assumption implies that mass transfer rate at the vapor-liquid interface is infinitely fast. Such models have been mostly implemented in density-based algorithms, with different approaches to derive the pressure-density relation. When the flow temperature variations are not significant, the EoS can be independent of temperature, which simplifies the pressure-density relations that can be typically expressed with a so-called barotropic EoS. Barotropic models can be implemented in both density-based and pressure-based algorithms [3,28,29]. For instance, in [30] compared an incompressible pressure-based solver with a compressible density-based counterpart both employing barotropic cavitation models. They showed the necessity to consider fluid compressibility effects to correctly describe the cavity dynamics. Single-fluid EoS models typically require knowledge of the speed of sound in the liquid, vapour and mixture regimes; high grid resolution along with small time steps (i.e.  $\Delta t < 10^{-10}$  s) are needed for adequate prediction of a sharp interface and pressure wave propagation. As a consequence, these models are computationally expensive and usually applied to cavitating flows in small-scale geometries. An extension of these models can consider real-fluid EoS, which can consider the vapourization and condensation processes during phase-change over a wide range of pressures and temperatures. For example, the work of [31-35] introduced an explicit density-based solver coupled with real-fluid thermodynamic properties for n-dodecane to demonstrate heating effects in bubble-collapse cases. The algorithm presented in the present work represents an extension of these works both in terms of numerical analysis and thermodynamic closure for cavitating flows. The in-house developed code is capable of capturing both small scale (i.e. single bubble cavitation and bubble interface movement) and full scale cavitation (i.e. cluster of bubble cavitation, with bubbles collapse interaction and vaporization among them). This is one of the first works implementing the Mach consistent numerical flux in conjunction with real-fluid properties for different fuels, demonstrating heating effects in bubble collapse cases and in-nozzle flow problems. The only relevant work is that reported in [36], who focused on water/vapour behaviour in benchmark (e.g. shock tube, explosion/implosion, forward step) and macroscopic (e.g. hydrofoil) cases and the work of [31,35] that focused on n-dodecane. This numerical framework is also suitable for the study of cavitation under DFICE operating conditions and allows us to assess how different fuels behave under such conditions.

### Computational Methodology

The presented methodology has been developed in OpenFOAM and was based on the code developed by the authors' group, as presented in [31]. As a reference within this manuscript, the new solver has been labelled as tabFoam. The governing equations of the compressible solver are given in the Euler form and comprise continuity, momentum and energy conservation along with a transport equation for the vapour mass fraction. Under the assumption that bubble growth and collapse are inertia-driven processes [37], viscosity and surface tension are neglected, and the governing equations are expressed as follows:

$$\frac{\partial \vec{q}}{\partial t} + \frac{\partial F_i(\vec{q})}{\partial x_i} = 0 \quad (1)$$

where  $\vec{q}$  is the vector of conserved variables:

$$\vec{q} = \begin{cases} \rho \\ \rho Y \\ \rho u_1 \\ \rho u_2 \\ \rho u_3 \\ E \end{cases} \quad (2)$$

and  $F$  is the vector of fluxes, defined as:

$$F(\vec{q}) = \rho u_i \begin{bmatrix} 1 \\ Y \\ u_1 \\ u_2 \\ u_3 \\ E \end{bmatrix} + p \begin{bmatrix} 0 \\ 0 \\ \delta_{1i} \\ \delta_{2i} \\ \delta_{3i} \\ u_1 \end{bmatrix} \quad (3)$$

where  $\rho$  is the fluid density,  $Y$  is the mass fraction,  $u_i$  is the  $i$ -th component of the velocity vector,  $p$  is pressure,  $\delta_{1i}$  denotes the Kronecker symbol, and  $E$  is the specific total energy, which is the sum of the specific internal energy and the specific kinetic energy. In addition to that, the thermodynamic closure used in this methodology is based on the Helmholtz energy EoS [38], which can provide thermodynamic properties at sub-critical and supercritical conditions in a consistent framework. In this framework, the Homogeneous Equilibrium Mixture (HEM) approach is used, where each thermodynamic property can be expressed as a function of density, internal energy and mass fraction. Therefore, the EoS for calculating the thermodynamic properties of the working fluid is expressed using the Helmholtz energy, having as independent variables density and temperature:

$$\alpha(\rho, T) = \alpha^0(\rho, T) + \alpha^r(\rho, T) \quad (4)$$

Subsequently, Eq. 4 can be expressed in a dimensionless manner:

$$\frac{\alpha(\rho, T)}{RT} = \alpha(\delta, \tau) = \alpha^0(\delta, \tau) + \alpha^r(\delta, \tau) \quad (5)$$

where  $\delta = \frac{\rho}{\rho_c}$  and  $\tau = \frac{T}{T_c}$  are, respectively, the dimensionless density and temperature with respect to relevant critical values. In particular,  $\alpha^0(\delta, \tau)$  is the dimensionless Helmholtz energy of the ideal gas while  $\alpha^r(\delta, \tau)$  is the residual Helmholtz energy. These 2 parameters, and in particular the latter, may be manipulated to obtain thermodynamic properties such as pressure  $p$ , internal energy  $e$ , enthalpy  $h$ , entropy  $s$ , and speed of sound  $c$  as a function of density  $\rho$  and temperature  $T$ . Additionally, saturation conditions are identified using the Maxwell criterion. In other words, liquid and vapour phases can be identified by solving Eqs. 8 and 9 for a given temperature:

$$p(\rho_{V,sat}, T_{sat}) = p(\rho_{L,sat}, T_{sat}) \quad (6)$$

$$g(\rho_{V,sat}, T_{sat}) = g(\rho_{L,sat}, T_{sat}) \quad (7)$$

where  $g$  stands for Gibbs Free Energy. Finally, we can define the properties within the saturation domain using the mixture assumption based on the volume fraction  $\alpha$ . An Example is given by the equation for the enthalpy:

$$\rho h = (1 - \alpha)h_{sat,L}\rho_{sat,L} + \alpha h_{sat,V}\rho_{sat,V} \quad (8)$$

Finally, the mixture speed of sound is determined by using the Wallis speed of sound's formula [39]. The procedure described by Eqs. 4-8 can be performed directly during code execution. However, it requires root finding of non-linear equations, since the Helmholtz energy is naturally expressed as a function of density  $\rho$  and temperature  $T$ , whereas tabFoam calculates density  $\rho$  and internal energy  $e$ , as shown in Eqs. 2 and 3. Moreover one would also need to find whether the flow is at saturation conditions or not, i.e., the algorithm needs to solve for the Maxwell criterion as well (Eqs. 6 and 7). In other words, at each time step the conservative variables  $(\rho, \rho E)$  must be transformed to  $(\rho, T)$  and then used to derive pressure and speed of sound for the next calculation step. This can be done, using, for example, the Newton–Raphson method, but it is very time consuming and inefficient. As a consequence, instead of solving the aforementioned EoS for each time step, a similar technique as the one employed in [36] has been developed. More specifically, a structured thermodynamic table computed prior to the simulations has been used. This table contains the physical properties as derived from the Helmholtz EoS for each single-component fluid (i.e., water, dodecane, methanol, and ethanol); multi-component fluid mixtures are not currently supported. The structured table is built by selecting an appropriate range for density and internal energy, which encloses the expected conditions of the bubble collapse simulation. A graphical representation of stored thermodynamic properties is shown in Fig. 1, whilst the size and resolution of the thermodynamic table are summarised in Table 1. It should be noted that it has been confirmed that the resulting algorithm is more efficient than the on-the-fly calculation of the Helmholtz EoS, by almost one order of magnitude in terms of computational time. During algorithm execution and after calculating the conservative vector in the time loop, and hence once density and internal energy (and mass fraction, in case there are more than one species in the simulation) are known, the element of the thermodynamic table in which each cell of the computational domain belongs is determined using a simple access operator and an interpolation method.

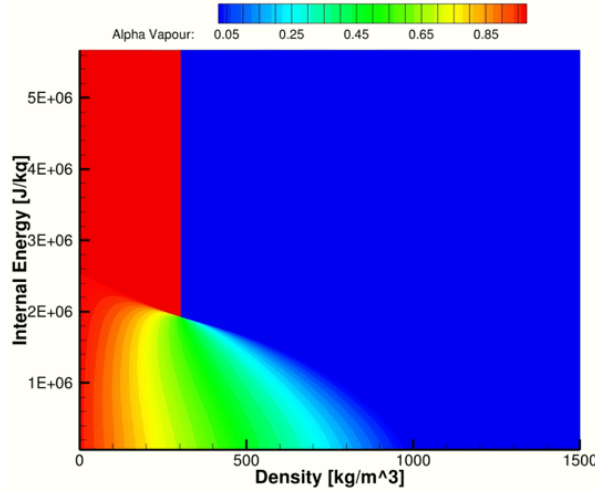


**Figure 1.** Contour plot of the thermodynamic properties of water, showing liquid and vapour areas depending on density, vapour fraction, and internal energy.

**Table 1.** Range definition for density and internal energy for the structured thermodynamic table developed for water.

Property	Min	Max	$\Delta$	Number of points
$\rho$ [kg/m <sup>3</sup> ]	0.001	2000	0.75	2000
$e$ [J/kg]	62266	5665387	1868.2	3000

Cavitation processes involve a large variation in the speed of sound and, thus, the Mach number changes significantly. For this reason, it is difficult to apply a unified discretization method suitable across the whole computational domain. In fact, the flow can be considered incompressible in the liquid regime, where the Mach number can be of the order of  $10^{-2}$ . On the other hand, in the liquid-vapor mixture regime the flow is highly compressible and the Mach number can be of the order of  $10^2$  or even higher, due to the small speed of sound in the two-phase mixture. When using density-based solvers for low Mach number flows, slow convergence and incorrect solutions have been noticed [37]. To overcome this, a Mach-consistent numerical flux based on the work of [42] has been implemented, which is based on the HLLC flux and the AUSM flux. Thus, the numerical flux at the  $i+1/2$  interface takes the form:

$$F(\vec{q}) = \rho_{L/R} u_{face} \begin{bmatrix} 1 \\ Y \\ u_{L/R} \\ u_{L/R} \\ E_{L/R} \end{bmatrix} + p_{face} \begin{bmatrix} 0 \\ 0 \\ 1 \\ 0 \\ 0 \\ u_{face} \end{bmatrix} \quad (9)$$

where  $u_{face}$  and  $p_{face}$  are given by Eq. 16 and 17 respectively:

$$u_{face} = \frac{\rho_L c_L u_L + \rho_R c_R u_R + p_L - p_R}{\rho_L c_L + \rho_R c_R} \quad (10)$$

$$p_{face} = (1 - b)p^{inc} + bp^{comp} \quad (11)$$

where the incompressible and compressible pressure value component and  $b$  are shown in Eqs. 18, 19 and 20 respectively:

$$p^{inc} = \frac{\rho_L c_L p_R + \rho_R c_R p_L}{\rho_R c_R + \rho_L c_L} \quad (12)$$

$$p^{comp} = \frac{\rho_L c_L p_R + \rho_R c_R p_L + \rho_L c_L \rho_R c_R (u_L - u_R)}{\rho_R c_R + \rho_L c_L} \quad (13)$$

$$b = 1 - e^{-dMa} \quad (14)$$

$$Ma = \max\left(\frac{|u_L|}{c_L}, \frac{|u_R|}{c_R}\right) \quad (15)$$

Where  $\rho_{L/R}$ ,  $u_{L/R}$  and  $E_{L/R}$  depend on the sign of  $u_{face}$ . The value of the left-hand-side cell is taken when the sign of  $u_{face} > 0$  and vice versa. Moreover,  $d$  is the blending coefficient whose value is between 1 and 100 [35]. In order to achieve 2<sup>nd</sup> order accuracy in space, the MUSCL reconstruction [40, 41] is employed to determine conservative variables at cell interfaces, which in turn are used for the flux estimation. Moreover, since the cavitation phenomena simulated are unsteady, a four stage Runge-Kutta method, 2<sup>nd</sup> order in time has been implemented [40].

$$\frac{\partial \vec{U}}{\partial t} = \vec{R}(t, \vec{U}) \quad (16)$$

$$\vec{U}(t_0) = \vec{U}_0 \quad (17)$$

Finally, the numerical solution of this differential equation is solved by using a RK4 method. This specific RK method was selected since it has low storage requirements and only the solution vectors from time  $n$  and  $n + 1$  need to be stored, which is important for large scale simulations.

## Results and discussion

In this section, various results obtained for validation of the developed solver are presented. The first flow scenario examined is the single spherical bubble (radius  $R = 400\mu\text{m}$ ) collapsing in an infinite medium [22] under compression due to the higher pressure of the surrounding liquid. Taking advantage of the spherical symmetry, a 2D geometry was employed for this simulation, with the use of a wedge-type numerical grid. The bubble's centre is located at the origin, i.e. at  $x = 0$ ,  $y = 0$ , and  $z = 0$ . The computational domain extends 50 times the size of the initial vapour radius (i.e., 8 mm from the centre of the bubble) in order to minimize the interference with the boundaries. In addition to that, the mesh is refined at the bubble region (defined to be 2.5 times the radius of the bubble) where 1,000 equally spaced cells have been used, while a stretching ratio of 1.05 with 1,000 cells has been used outside the bubble. A wave transmissive boundary condition has been used at the far-field right-hand-side and a symmetry condition was selected for the left side, in order to simulate the axis of the wedge (Fig. 2 and 3).

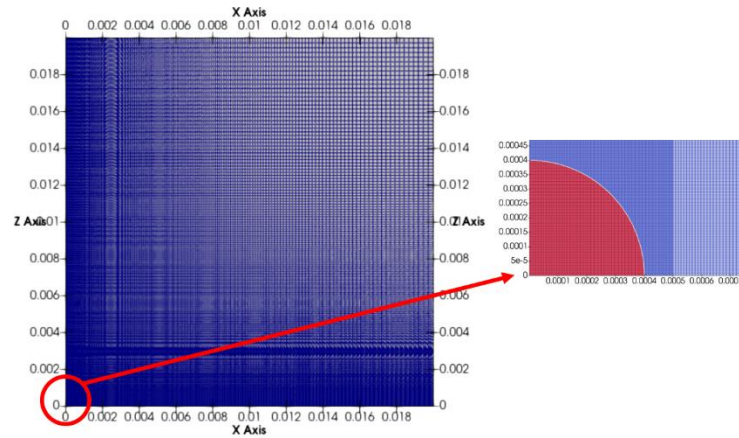


Figure 2. X-Z plane view of the geometry for the Rayleigh bubble collapse case.

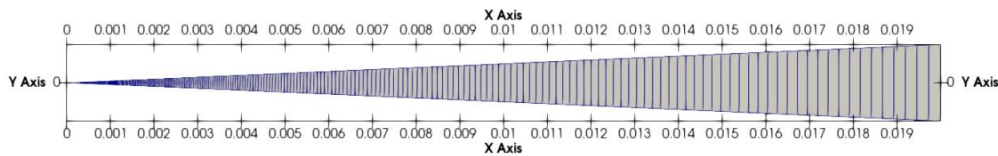


Figure 3. X-Y plane view of the geometry for the Rayleigh bubble collapse case.

The fluid is pure dodecane and the initial conditions for this case are summarised in Table 2.

Table 2. Initial conditions for the case of Rayleigh Bubble Collapse.

Variable	Vapour Condition	Liquid Condition
$\rho$ [kg/m <sup>3</sup> ]	0.0015	744.36
$e$ [J/kg]	-142760	-488540

p [Pa] | 19.64                      101325

According to [22], the inertial bubble collapse velocity is given by:

$$\frac{dR}{dt} = -\sqrt{\frac{2(p_{inf} - p_{vap})}{3\rho_{liq}} \left[ \left(\frac{R_0}{R}\right)^3 - 1 \right]} \quad (18)$$

Then the characteristic Rayleigh time  $\tau$ , that can be defined as the time a bubble needs to collapse, or to reach its minimum volume, under specific conditions, is defined as:

$$\tau = 0.915R_0 \sqrt{\frac{\rho_{liq}}{p_{inf} - p_{vap}}} \quad (19)$$

For the specific configuration, the characteristic Rayleigh time is calculated equal to  $\tau = 31.5\mu\text{s}$ . As shown in Fig. 4, the comparison between the semi-analytical solution and the numerical predictions is satisfactory.

At a second step, the collapse of a cluster of bubbles over a flat wall is considered. Initially, simulations are performed utilising the properties of water; the results are compared against those [42] and [27]. Following, simulation of a cluster of bubble for 3 different fuels has been performed revealing the effect of fuel properties on the pressure peaks occurring during the collapse of the cloud.

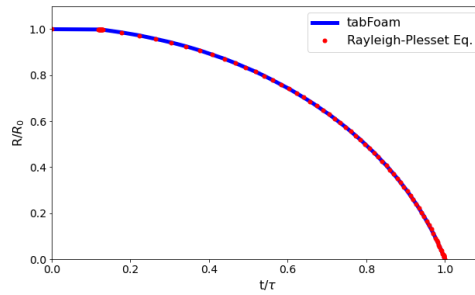


**Figure 4.** Normalised bubble radius evolution with respect to normalised time with the Rayleigh bubble collapse timescale  $\tau$ .

The bubble cloud consists of 125 spherical vapor bubbles; their radius distribution ranges from 0.70 mm to 1.64 mm in a non-uniform manner (the actual distribution is given in [42]). The mean bubble radius is 0.95mm, while the minimum distance among them is 0.2mm. Moreover, the bubbles have larger concentration and radii around the centre of the cloud. The overall cloud is located in a small liquid-filled cubic domain of  $20 \times 20 \times 20 \text{ mm}^3$  and correspond to a total volume fraction of 5.8%. The cubic domain, itself, is located in a larger rectangular domain of  $4 \times 4 \times 2 \text{ m}^3$ ; the bottom face of the two domains are co-planar. The initial bubble distribution inside the inner domain is depicted in Fig. 5.

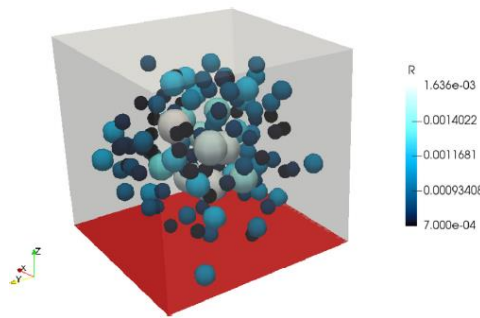
The liquid containing the bubbles is assumed to be stagnant with a uniform temperature of 293 K. The initial pressure inside the bubbles is set equal to the vapour pressure of 2,340 Pa while in the surrounding liquid it is assumed to have a Laplacian distribution that is shown in eq. 20.

$$P(r, t = 0) = p_{sat,l} + \Delta p \frac{r - R_0}{r} \quad \text{for } r > R_0 \quad (19)$$

This Laplacian distribution for pressure, as extensively reported in literature, is reasonable for stationary conditions since the smooth transition from vapour pressure and high pressure liquid condition is more realistic. The co-planar bottom faces of the two numerical domain are defined as impermeable walls; the other outer faces are considered as far-field boundaries with constant pressure of  $4 \cdot 10^6 \text{ Pa}$  and zero gradients for all other flow parameters. Finally, in order to estimate an average pressure induced by the collapsing bubbles on the bottom wall, one virtual 'pressure transducer' is considered at the centre of the bottom face. The integration area is  $1 \text{ cm}^2$  while the average pressure over this area is calculated at every computational time step. As there are no experimental data or analytical solution for this problem, comparison against the numerical predictions of [27] and [42] are presented.

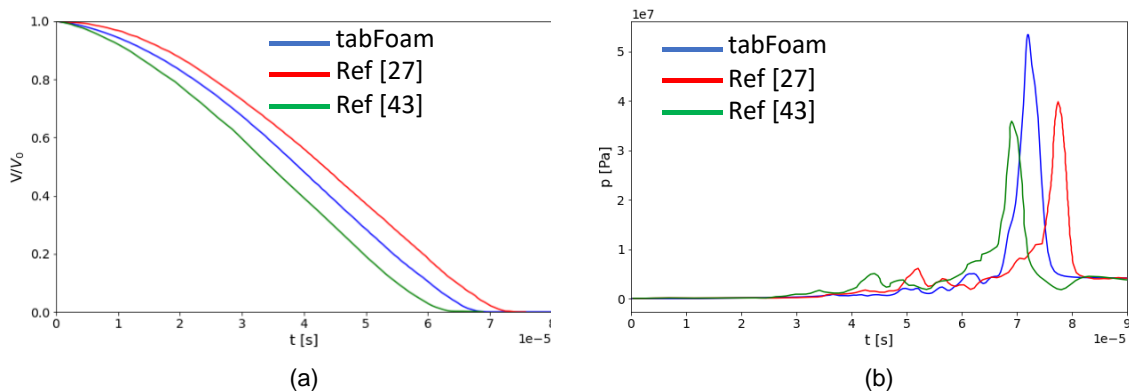
In particular, the authors of [27] are utilising an Eulerian–Lagrangian cavitation model based on the coupling of an Eulerian finite mass transfer model and a bubble tracking Lagrangian model. The vapour–liquid mixture properties are obtained based on a volume fraction methodology. Thermodynamic closure is obtained by using the ideal gas law for the pure vapour phase, and the modified Tait EoS for the liquid. In [42] instead, they utilised their inhouse

code (CATUM); this algorithm is very similar to the one proposed here, but the thermodynamic closure is obtained through a barotropic model.



**Figure 5.** Representation and distribution of 125 spherical non-intersecting bubbles over a flat wall (red surface)[27].

As shown in Fig.6a, the collapse time of the cloud in the simulations of reported in [27, 43] is equal to  $7.3 \cdot 10^{-5}$  s and  $6.3 \cdot 10^{-5}$  s, respectively. The respective time in the current work is  $6.9 \cdot 10^{-5}$  s. Overall, the estimated collapse time shows good agreement between the different modelling approaches. The time shift between the three simulations could be owed to the different thermodynamic models employed or due to minimal differences in the initial pressure field of the simulations.



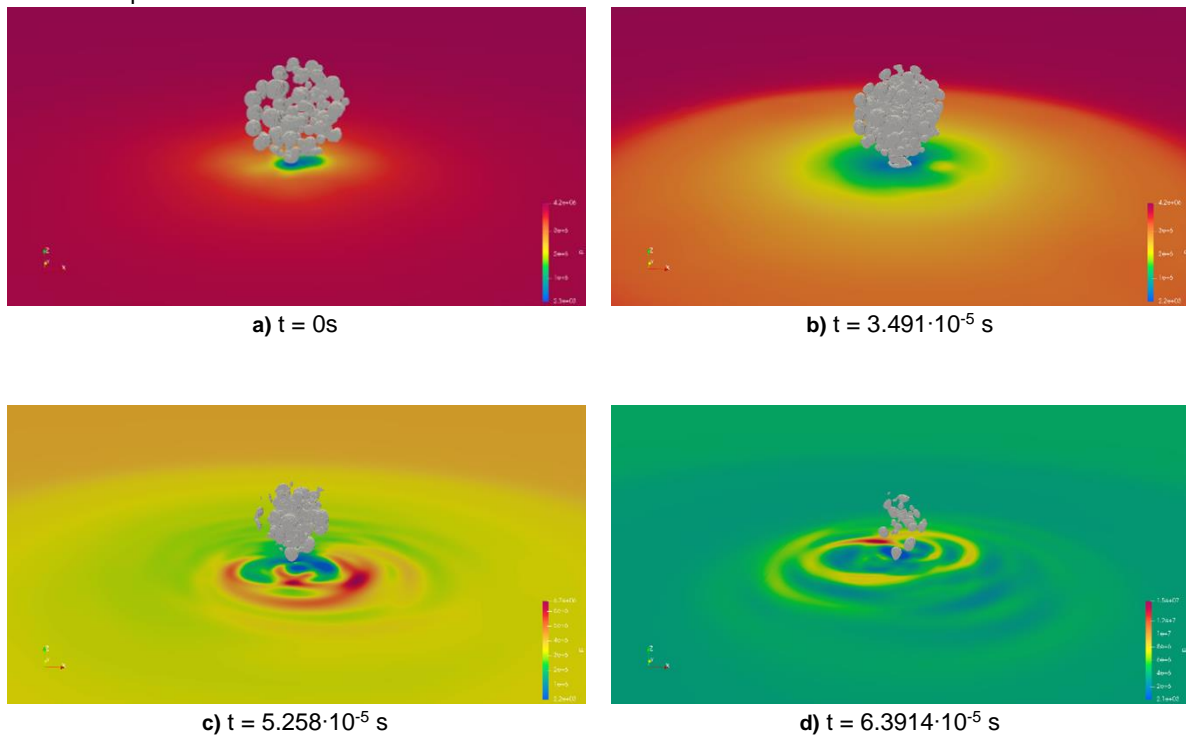
**Figure 6.** Validation of tabFoam simulation of bubble cluster against published data; (a) time history of the vapour volume; (b) average pressure on the wall transducer.

Fig. 6b shows the comparison of the average pressure recorded on the ‘virtual transducer’ (as defined in the previous paragraph). A small difference in peak pressure values can be discerned, which is due to the different flux schemes used in the simulations (this, of course, is also a reason for the difference in the time to collapse Fig. 6a). However, all pressure peaks have the same order of magnitude. Finally, Fig. 7 shows the bubble cloud topology (i.e. iso-surfaces created by setting the volume fraction = 0.5) and wall pressure contours at different time instances; these visualisations give an overview of the time evolution of the bubble cluster collapse.

Fig. 7a shows the initial position of the bubbles and the pressure induced on the wall. Fig. 7b illustrates the collapse of the cloud of bubble at  $t = 3.491 \cdot 10^{-5}$  s; the bubbles located at the periphery of the cloud start collapsing first. It is evident that the collapse of the cloud is progressing towards its centre. Fig. 7c corresponds to a time step where the peripheral bubble have collapsed and those located at the centre of the cloud are following; the induced jets forming at the centre of each collapsing bubble start to impact on the wall underneath the cluster, as evidenced by the increased pressure distribution on the wall. Finally, Fig. 7d corresponds to a time instance at the latest stage of the collapse, where all the pressure distribution on the wall exhibits a ring structure.

Having established the flow and bubble cluster collapse process for water, we proceed now to simulations where collapse of bubble clouds in various fuels have been simulated. Following the test case reported in [43], the cloud consists of 150 spherical vapor bubbles with a constant radius equal to  $1.5 \cdot 10^{-3}$  m; similar to the previous case, the minimum distance among bubbles is of  $0.2 \cdot 10^{-3}$  m to avoid intersection and they have larger concentration around the centre of the cloud. The overall cloud is located in a small liquid-filled spherical domain of radius  $15 \cdot 10^{-3}$  m with a stand-off distance from the wall of  $3.2 \cdot 10^{-3}$  m, and has an average vapour volume fraction of 8%.

This smaller domain, itself, is located in a larger rectangular domain of  $4 \times 4 \times 2 \text{ m}^3$  and the bottom faces of the two domains are co-planar. The numerical set-up is common for all fuels examined. Table 3 summarises the conditions referring to the flow far field, whilst Table 4 shows those relevant to the cluster of bubbles. The far field has been initialized with 10 MPa and 350K, while the bubbles have been initialised with a temperature of 350 K at their saturation vapor conditions.



**Figure 7.** Bubble cloud topology (i.e. iso-surfaces created by setting the volume fraction = 0.5) and wall pressure contours at different time instances: (a)  $t = 0 \text{ s}$ , (b)  $t = 3.491 \cdot 10^{-5} \text{ s}$ , (c)  $t = 5.258 \cdot 10^{-5} \text{ s}$ , and (d)  $t = 6.3914 \cdot 10^{-5} \text{ s}$ .

From Table 3 it is evident that at the same conditions, dodecane has a lower density and, similarly, Table 4 shows that dodecane (at saturation conditions) has a significantly lower vapor pressure compared to methanol and ethanol, suggesting a lower tendency to cavitate. Finally, in order to compare the resulting pressure and temperature peaks from the three fuels, the maximum pressure and temperature at the ‘virtual transducer’ located on wall below the bubble cluster, as well as the in the whole computational domain have been considered.

**Table 3.** Far-field initial conditions for the examined fuels.

Fuel	$\rho$ [kg/m <sup>3</sup> ]	$e$ [J/kg]	$p$ [Pa]	$T$ [K]
Dodecane	714	-378040.1	$100 \cdot 10^5$	350
Ethanol	749.5	403889.3	$100 \cdot 10^5$	350
Methanol	748.2	29389.2	$100 \cdot 10^5$	350

**Table 4.** Initial conditions for each vaporous bubble for the examined fuels.

Fuel	$\rho$ [kg/m <sup>3</sup> ]	$e$ [J/kg]	$p$ [Pa]	$T$ [K]
Dodecane	2.6	-369052.8	614.2	350
Ethanol	2.9	831458	95220.6	350
Methanol	1.45	1042157.2	125889.8	350

Initially, the equivalent bubble cluster radii evolution for the three fuels is compared; this has been obtained by summing the volume for all the 150 bubbles and finding the radius of a single bubble with the total volume just obtained. It is clear that fuel properties do not influence considerably the collapse time of the cluster of bubbles. The dodecane bubble collapses about  $10^{-6} \text{ s}$  earlier compared to the two alcohol bubble clusters as shown in Fig. 8; this is attributed to the lower initial pressure of the vaporous cluster of bubbles (i.e. the vapour pressure as expressed in Tab. 4).

Moreover, it can be noted that out of the three fuel at the initial conditions (i.e. temperature 350 K and pressure 10 MPa), methanol has the largest latent heat (1,070 J/kg) compared to ethanol (852,3 J/kg) and dodecane (332.8 J/kg). So, during collapse the condensation processes results to higher methanol liquid temperature, as also shown in Fig. 9 and 10. Also, methanol, shows the strongest compression heating compared to the other two liquids tested, and this is clearly visible in Fig 10b and 11b, where methanol reaches higher temperatures both at the wall and inside the domain.

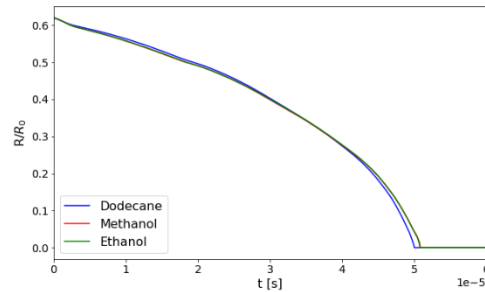


**Figure 8.** Bubble cluster equivalent radii time evolution comparison among dodecane, methanol and ethanol.

In fact, methanol's temperature increase as pressure rises for constant entropy is larger than the other fuels and this is also confirmed in the simulations as shown in Fig. 10a and 10b. In the same way, it is evident from tables 3 and 4 that dodecane has the lowest heat of vaporization and density at saturation conditions and, once again, this reflects on the trends obtained in the simulations.

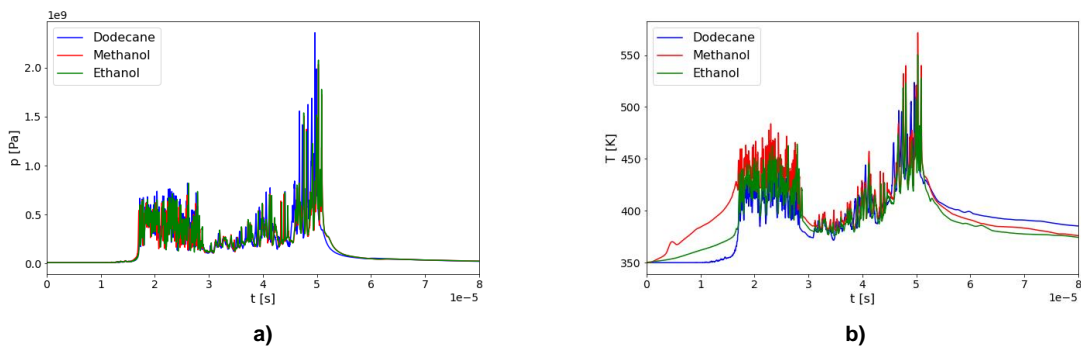


**Figure 9.** Maximum (a) pressure and (b) temperature in the whole computational domain for dodecane, methanol, and ethanol.

Finally, from Figs. 9a and 10a it can be inferred that dodecane shows a stronger collapse (i.e., higher pressure peaks). This is imputable to a higher level of condensation with respect to the other fuels. Moreover, dodecane's bubble cluster collapses faster as it is lighter (i.e. has a lower density at the same conditions) compared to the other fuels and this would bring to higher pressure (Fig. 11a and 11b) as a consequence of the more violent and faster collapse. As a consequence, dodecane is shown to have might create more issues when studying cavitation and cavitation-induced erosion..

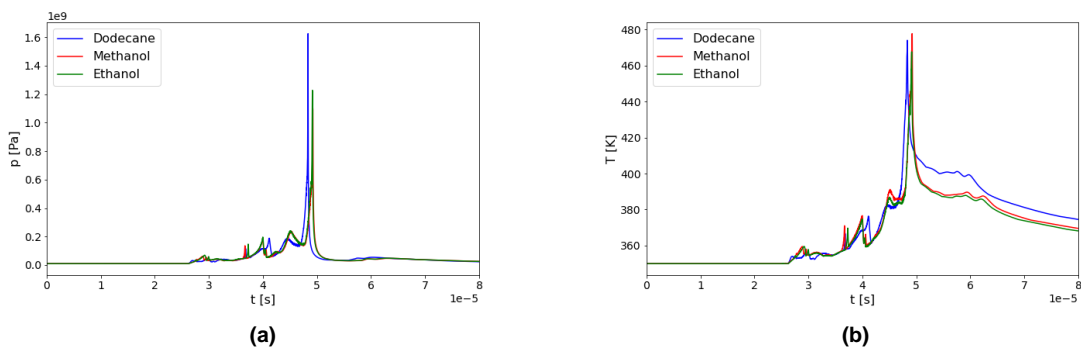


**Figure 10.** Maximum (a) pressure and (b) Temperature at the wall for Dodecane, Methanol, and Ethanol

## Conclusions

The CFD solver tabFoam has been developed and implemented in OpenFOAM and used to simulate test-cases of relevance to collapse of cluster of bubbles at conditions relevant to those prevailing in high pressure fuel injection nozzles utilised with dual fuel internal combustion engines. The code has been validated against analytical solutions and prior published numerical results. In particular, it has been firstly compared against the Rayleigh-Plesset equation for isolated bubble in an infinite liquid. Subsequently the predictive capability of the solver has been verified in a numerical case referring to a cluster of bubbles collapsing close to a wall, showing similar performance compared to published numerical data. Following, results from the collapse of a bubble cloud of three different fuels has been simulated. The results show some differences on the pressures and temperatures developing on nearby wall, but with overall minimal differences with regards to collapse times and mean temperatures.

## Acknowledgements

This project has received funding from the European Union's Horizon 2020 research and innovation programme under the Marie Skłodowska-Curie projects No 861002 (EDEM) and No 101028449 (AI-FIE).

## Nomenclature

and	Arbitrary Values	$p_{\text{face}}$	Pressure at the Cell Face
1D	One-Dimension	R	Universal Gas Constant
2D	Two-Dimension	R	Bubble Radius
3D	Three-Dimension	R0	Initial Radius
AUSM	Advection Upstream Splitting Method	RK	Runge-Kutta
c	Speed of Sound	s	Entropy
CFD	Computational Fluid Dynamics	T	Temperature
Cp	Specific Heat at Constant Pressure	u	Velocity
Cv	Specific Heat at Constant Vapour	$u_{\text{face}}$	Velocity at the Cell Face
d	Blending Coefficient	Y	Mass fraction
DBM	Discrete Bubble Model	$\alpha$	Volume Fraction
DFICE	Dual Fuel Internal Combustion Engine	$\rho$	Density
E	Specific Total Energy	$\vec{q}$	Vector of conserved Variables
e	Internal Energy	$\delta$	Kroneker Symbol
EoS	Equation of State	$\alpha(\rho, T)$	Helmholtz Energy
$F(\vec{q})$	Vector of fluxes	$\alpha^0(\delta, \tau)$	Helmholtz Energy of Ideal Gas
FMT	Finite Mass Transfer	$\alpha^r(\delta, \tau)$	Residual Helmholtz Energy
g	Gibbs Free Energy	$\delta$	Dimensionless density
h	Enthalpy	$\tau$	Dimensionless Temperature
HEM	Homogeneous Equilibrium Mixture	$T_c$	Critical Temperature
HLLC	Harten-Lax-van Leer-Contact	$\rho_c$	Critical Density
i	i-th component	$T_{\text{sat}}$	Saturation Temperature
Ma	Mach Number	$\rho_{L,\text{sat}}$	Density at Liquid Saturation Condition
MUSCL	Monotonic Upstream-centered Scheme for Conservation Laws	$\rho_{V,\text{sat}}$	Density at Vapour Saturation Condition
p	Pressure		

## References

- [1] H.R. Reitz, H. Ogawa, R. Payri, T. Fansler, S. Kokjohn, Y. Moriyoshi, A.K. Agarwal, D. Arcoumanis, D. Assanis, C. Bae, K. Boulouchos, M. Canakci, S. Curran, I. Denbratt, M. Gavaises, M. Guenther, C. Hasse, Z. Huang, T. Ishiyama, B. Johansson, T.V. Johnson, G. Kalghatgi, M. Koike, S.C. Kong, A. Leipertz, P. Miles, R. Novella, A. Onorati, M. Richter, S. Shuai, D. Siebers, W. Su, M. Trujillo, N. Uchida, B.M. Vaglieco, R.M. Wagner, H. Zhao 'IJER editorial: The future of the internal combustion engine', International Journal of Engine Research, 2019, <https://doi.org/10.1177/1468087419877990>
- [2] Onorati A, Payri R, Vaglieco B, Agarwal A, Bae C, Bruneaux G, Canakci M, Gavaises M, Günthner M, Hasse C, Kokjohn S, Kong S-C, Moriyoshi Y, Novella R, Pesyridis A, Reitz R, Ryan T, Wagner R, Zhao H, 'The Role of Hydrogen for Future Internal Combustion Engines', Int J Engine Research, 2022; <https://doi.org/10.1177/14680874221081947>
- [3] E. Gomez Santos, J. Shi, R. Venkatasubramanian, G. Hoffmann, M. Gavaises, W. Bauer 'Modelling and prediction of cavitation erosion in GDI injectors operated with E100 fuel', FUEL, Vol 289, 119923, 2021; <https://doi.org/10.1016/j.fuel.2020.119923>.
- [4] P. Koukouvinis, N. Mitroglou, M. Gavaises, M. Lorenzi, M. Santini 'Quantitative predictions of cavitation presence and erosion-prone locations in a high pressure cavitation test rig', Journal of Fluid Mechanics, vol 817, pp 21-57, 2017; <https://doi.org/10.1017/jfm.2017.156>
- [5] M. Cristofaro, W. Edelbauer, P. Koukouvinis and M. Gavaises, "A numerical study on the effect of cavitation erosion in a diesel injector," Applied Mathematical Modeling, vol. 78, pp. 200-216, 2020, doi: <https://doi.org/10.1016/j.apm.2019.09.002>.
- [6] P. Koukouvinis, N. Mitroglou, M. Gavaises, M. Lorenzi and M. Santini, "Quantitative predictions of cavitation presence and erosion-prone locations in a high-pressure cavitation test rig," Journal Fluid Mechanics, vol. 819, pp. 21-57, 2017,

- doi: 10.1017/jfm.2017.156.
- [7] M. Brunhart, C. Soteriou, C. Daveau, M. Gavaises, P. Koukouvinis & M. Winterbourn 'Cavitation erosion risk indicators for a thin gap within a diesel fuel pump', *Wear*, 203024, 2019; <https://doi.org/10.1016/j.wear.2019.203024>.
- [8] C. Arcoumanis, M. Badami, H. Flora and M. Gavaises 'Cavitation in real size multi-hole diesel injector nozzles', *Transactions Journal of Engines*, SAE Paper 2000-01-1249, Vol. 109-3, 2000; <https://doi.org/10.4271/2000-01-1249>
- [9] Chaves H, Knapp M, Kubitzek A, Obermeier F, Schneider T 'Experimental study of cavitation in the nozzle hole of diesel injectors using transparent nozzles. SAE technical paper 950290. doi: 10.4271/950290
- [10] B.A. Reid, M. Gavaises, N. Mitroglou, G.K. Hargrave, C.P. Garner, E.J. Long, R.M. McDavid 'On the formation of string cavitation in Diesel injectors', *Experiments in Fluids*, 55:1662, 2014; <https://doi.org/10.1007/s00348-013-1662-8>
- [11] M. Gavaises, "Modeling of Diesel fuel injection processes," PhD Thesis, Imperial College London, 1997.
- [12] M. Gavaises, Mithun Girija Murali, P. Koukouvinis, M. Gold and R. Pearson 'Numerical simulation of fuel dribbling and nozzle wall wetting', *Int Journal Engine Research*, Vol. 23(1) 132–149, 2021, <https://doi.org/10.1177/1468087420985189>
- [13] O. Baran, I.K. Karathanassis, P. Koukouvinis, J. Hwang, L.M. Pickett, D. Spivey, M. Gavaises 'Assessment of injector-flow characteristics of additised and renewable diesel blends through high-speed imaging', *FUEL*, vol 352, pp 129076, 2023; <https://doi.org/10.1016/j.fuel.2023.129076>
- [14] M. Heidari-Koochi, I.K. Karathanassis; P. Koukouvinis; J. Hwang; Lyle M. Pickett, D. Spivey, M. Gavaises 'Flow visualisation in real-size optical injectors of conventional, additised, and renewable gasoline blends', *Energy Conversion and Management*, 252, 115109, 2022; <https://doi.org/10.1016/j.enconman.2021.115109>
- [15] I. Malgarinos, N. Nikolopoulos and M. Gavaises, "Coupling a local adaptive grid refinement technique with an interface sharpening scheme for the simulation of two-phase flow and free-surface flows using VOF methodology," *Journal Computational Physics*, vol. 300, pp. 732–753, 2015, <https://doi.org/10.1016/j.jcp.2015.08.004>.
- [16] I. Malgarinos, N. Nikolopoulos and M. Gavaises, "Numerical investigation of heavy fuel droplet-particle collisions in the injection zone of a Fluid Catalytic Cracking reactor, Part I: Numerical model and 2D simulations," *Fuel Processes Technology*, vol. 156, pp. 317–330, 2017, doi: 10.1016/j.fuproc.2016.09.014.
- [17] C. Wang, M. Adams, T. Luo, T. Jin, F. Luo and M. Gavaises, "Hole-to-hole variations in coupled flow and spray simulation of a double-layer multi-holes diesel nozzle," *International Journal Engine Research*, vol. 22, no. 10, pp. 3233–3246, 2021, <https://doi.org/10.1177/1468087420963986>.
- [18] A. K. Singhal, M. M. Athavale, H. Li, and Y. Jiang, "Mathematical basis and validation of the full cavitation model," *Journal Fluids Engineering Transactions ASME*, vol. 124, no. 3, pp. 617–624, 2002, <https://doi.org/10.1115/1.1486223>.
- [19] E. Lauer, X. Y. Hu, S. Hickel and N. A. Adams, "Numerical modelling and investigation of symmetric and asymmetric cavitation bubble dynamics," *Comput. Fluids*, vol. 69, pp. 1–19, 2012, doi: 10.1016/j.compfluid.2012.07.020.
- [20] M. Cristofaro, W. Edelbauer, P. Koukouvinis, M. Gavaises 'Large Eddies Simulation of the injector internal flow during a pilot injection', CAV2018, Baltimore, 14-16 May 2018; [https://doi.org/10.1115/1.861851\\_ch127](https://doi.org/10.1115/1.861851_ch127)
- [21] G. H. Schnerr and J. Sauer, "Physical and Numerical Modeling of Unsteady Cavitation Dynamics," *4th Int. Conf. Multiphase Flow*, pp. 1–12, 2001.
- [22] J.P. Frank and J.M. Michel *Fundamentals of Cavitation*, Springer, 2005
- [23] P. Koukouvinis, M. Gavaises, O. Supponen, and M. Farhat, "Numerical simulation of a collapsing bubble subject to gravity," *Physics of Fluids*, vol. 28, no. 3, 2016, <https://doi.org/10.1063/1.4944561>.
- [24] S. Yakubov, T. Maquil, and T. Rung, "Experience using pressure-based CFD methods for Euler-Euler simulations of cavitating flows," *Computers and Fluids*, vol. 111, pp. 91–104, 2015, <https://doi.org/10.1016/j.compfluid.2015.01.008>.
- [25] E. Giannadakis, M. Gavaises and C. Arcoumanis 'Modelling of cavitation in Diesel injector nozzle holes', *Journal of Fluid Mechanics*, Vol 616, pp 153-193, 2008; <https://doi.org/10.1017/S0022112008003777>
- [26] Ziyang Wang, Huaiyu Cheng, Rickard E. Bensow, Xiaoxing Peng, Bin Ji 'Numerical assessment of cavitation erosion risk on the Delft twisted hydrofoil using a hybrid Eulerian-Lagrangian strategy, *International Journal of Mechanical Sciences*, Vol 259, 108618, 2023. <https://doi.org/10.1016/j.ijmecsci.2023.108618>.
- [27] E. Ghahramani, M. H. Arabnejad, and R. E. Bensow, "A comparative study between numerical methods in simulation of cavitating bubbles," *Int. J. Multiph. Flow*, vol. 111, pp. 339–359, 2019, <https://doi.org/10.1016/j.ijmultiphaseflow.2018.10.010>.
- [28] T. Lyras, I.K. Karathanassis, N. Kyriazis, P. Koukouvinis and M. Gavaises 'Modelling of liquid oxygen nozzle flows under subcritical and supercritical pressure conditions', *Int J Heat Mass Transfer*, Vol 177, 121559, 2021; <https://doi.org/10.1016/j.jheatmasstransfer.2021.121559>
- [29] A. Papoutsakis, P. Koukouvinis and M. Gavaises 'Solution of cavitating compressible flows using Discontinuous Galerkin Discretisation', *Journal Computational Physics*, Vol 401, 109377, 2020; <https://doi.org/10.1016/j.jcp.2020.109377>
- [30] E. Goncalves, M. Champagnac, and R. F. Patella, "Comparison of numerical solvers for cavitating flows," *Int. J. Comput. Fluid Dyn.*, vol. 24, no. 6, pp. 201–216, 2010, <https://doi.org/10.1080/10618562.2010.521131>.
- [31] N. Kyriazis, P. Koukouvinis, and M. Gavaises, "Numerical investigation of bubble dynamics using tabulated data," *International Journal Multiphase Flow*, vol. 93, pp. 158–177, 2017, <https://doi.org/10.1016/j.ijmultiphaseflow.2017.04.004>.
- [32] P. Koukouvinis, C. Bruecker and M. Gavaises 'Unveiling the physical mechanism behind pistol shrimp cavitation', *Scientific Reports* 7, No 13994, 2017
- [33] N. Kyriazis, P. Koukouvinis, and M. Gavaises, "Modelling cavitation during drop impact on solid surfaces," *Advances in Colloids and Interface Science*, vol. 260, pp. 46–64, 2018, <https://doi.org/10.1016/j.cis.2018.08.004>.
- [34] E. Stavropoulos Vasilakis, N. Kyriazis, P. Koukouvinis, M. Farhat, and M. Gavaises, "Cavitation induction by projectile impacting on a water jet," *International Journal Multiphase Flow*, vol. 114, pp. 128–139, 2019, <https://doi.org/10.1016/j.ijmultiphaseflow.2019.03.001>.
- [35] N. Kyriazis, P. Koukouvinis, and M. Gavaises, "Numerical investigations on bubble-induced jetting and shock wave focusing: Application on a needle-free injection," *Proceedings Royal Society London A*, vol. 475, no. 2222, 2019, <https://doi.org/10.1098/rspa.2018.0548>.
- [36] M. Dumbser, U. Iben, and C. D. Munz, "Efficient implementation of high order unstructured WENO schemes for cavitating flows," *Computers and Fluids*, vol. 86, pp. 141–168, 2013, <https://doi.org/10.1016/j.compfluid.2013.07.011>.
- [37] D. P. Schmidt, C. J. Rutland, M. L. Corradini, P. Roosen, and O. Genge, "Cavitation in two-dimensional asymmetric nozzles," *SAE Technical Paper*, 1999, <https://doi.org/10.4271/1999-01-0518>.
- [38] E. W. Lemmon and M. L. Huber, "Thermodynamic Properties of n-Dodecane Thermodynamic Properties of n - Dodecane," *Energy & Fuels*, 2004, 18, 960-967, 2004

- [39] C. E. Brennen, *Cavitation and bubble dynamics*. Oxford University Press, New York, 1995.
- [40] E. F. Toro, *Riemann Solvers and Numerical Methods for Fluid Dynamics*. Springer, 2009.
- [41] Q. Wang, "Multi-oscillations of a bubble in a compressible liquid near a rigid boundary," *Journal Fluid Mechanics*, vol. 745, pp. 509–536, 2014, <https://doi.org/10.1017/jfm.2014.105>.
- [42] G. H. Schnerr, I. H. Sezal, and S. J. Schmidt, "Numerical investigation of three-dimensional cloud cavitation with special emphasis on collapse induced shock dynamics," *Physics of Fluids*, vol. 20, no. 4, 2008, <https://doi.org/10.1063/1.2911039>.
- [43] D. Ogloblina, S. J. Schmidt, and N. A. Adams, "Simulation and analysis of collapsing vapor-bubble clusters with special emphasis on potentially erosive impact loads at walls," *EPJ Web Conf.*, vol. 180, 2018, <https://doi.org/10.1051/epjconf/201817002079>.